

Nuclear emulsion readout system HTS aiming at scanning an area of one thousand square meters

Masahiro Yoshimoto^{1†*}, Toshiyuki Nakano¹, Ryosuke Komatani¹, and Hiroaki Kawahara¹

¹*Graduate School of Science, Nagoya University, Furo-cho, Chikusa-ku, Nagoya 464-8602, Japan*

*E-mail: yoshimoto@flab.phys.nagoya-u.ac.jp

.....
Automatic nuclear emulsion readout system has made remarkable progress for almost 40 years since the original idea. After the success in its full application to large-scale neutrino experiment OPERA, much faster readout system HTS (Hyper Track Selector) have been developed. The HTS, which has a extremely wide field objective lens, reached a scanning speed of 4700 cm²/h which is nearly 100 times faster than the previous system, and therefore is strongly promoting a lot of new experimental projects. We will describe the concept, specifications, system structure, and achieved performance in this paper.
.....

Subject Index H01, H34

1. Introduction

Nuclear emulsion is a three-dimensional particle tracking detector with a sub-micron spatial resolution. It has been used for cosmic ray research, and contributed to the discoveries of π -meson [1] and charmed particles [2]. In order to recognize the recorded trajectory with sub-micron accuracy, in those cosmic-ray experiments, the emulsion films were scanned by eyes under microscopes. Consequently, this time consuming method strongly limited the statistics. To improve this situation, automatic nuclear emulsion readout system, named Track Selector, has been developed in Nagoya University [3][4][5] and applied to many high energy experiments, WA75 [6], E653 [7], E176 [8], CHORUS [9] and DONUT [10]. Especially in DONUT, the readout system has achieved the discovery of τ neutrino. Thanks to the experiment, the validity of automatic nuclear emulsion readout system was demonstrated. In 2006, S-UTS with the readout speed of ~ 100 m²/year/system was released [11] to organize a large scale neutrino oscillation experiment, OPERA [12]. Adding to S-UTS, a similar readout system was also developed in Europe [13]. In the OPERA analysis of more than five years, the scanning area by those readout systems reached to the order of 100 m², and consequently, the systems have contributed to the discovery of $\nu_\mu \rightarrow \nu_\tau$ oscillation in appearance mode [14][15].

[†]Present Address: Physics Department, Faculty of Education, Gifu University, 1-1 Yanagido, Gifu 501-1193, Japan

The success of OPERA experiment, i.e. large area application of nuclear emulsion and automatic nuclear emulsion readout systems, leads a number of applications of nuclear emulsion technology, e.g. GRAINE project, NINJA project, cosmic-ray muon radiography project. GRAINE project [16][17] is aiming at a cosmic gamma-ray observation with balloon bone telescope. The angular resolution of nuclear emulsion is one order finer than that of Fermi LAT [18], so that the angular resolution allows the telescope to take sharper images of gamma-ray emission objects like supernova remnants. The scientific observation will be performed with multiple flights and large aperture $\sim 10 \text{ m}^2$ to be installed on a balloon. The test flights have already been carried out in 2011 and 2015 and observational flights using total area of 1000 m^2 nuclear emulsion are in its scope. NINJA project [19] is aiming at the precise measurements of low-energy neutrino-nucleus interactions and sterile neutrino search at J-PARC. Only the nuclear emulsion can detect short tracks and large angle tracks, i.e. low-energy charged particles like recoil protons, and nuclear evaporation fragment emitted to almost 4π region. Cosmic-ray muon radiography project is aiming at observing inner structures of large scale objects like volcanos, iron furnaces, nuclear power plants and archeological buildings like Pyramids. Nuclear emulsion has advantages in its compactness which includes no-requirement of power supply, and large angular acceptance. The nuclear emulsion has also a scalability, which realizes almost 100 times larger area than the other technologies such as a scintillation detector under a given cost.

In order to deal with those requirements for the experiments, we have been developing the next generation nuclear emulsion readout system aiming at readout speed of $\sim 1000 \text{ m}^2/\text{year}$, i.e. 100 times faster than S-UTS. In this paper, we will describe the HTS concept, basic configuration, evaluation of key devices, track detection performances, achieved readout speed, and future prospects to fulfill much faster system.

2. Automatic nuclear emulsion readout system and the concept of HTS

In nuclear emulsion, trajectories of charged particles are recorded as three-dimensionally aligned dots of developed silver grains. As shown in Fig. 1, the readout system takes tomographic images in an emulsion layer and recognizes those linked grains across the tomographic images as a track. A track finding algorithm of “Track Selector” searches especially straightly aligned dots, i.e. high momentum tracks.

Normally, the system is composed of a three-axis stage to scan the emulsion film, an objective lens to magnify the nuclear emulsion images, an image sensor for taking tomographic images, and dedicated processors and/or computers to process the acquired images and to manage the total system. The objective lens and the image sensor should satisfy the requirement of sub-micron resolution. In order to increase the readout speed, it is necessary to improve the performance of each device in a well-balanced way.

Fig. 2 shows the development of the readout speed of the Track Selector series. The most adequate digital technologies have been used at each moment to increase the processing speed. Angle acceptance has been also increasing every Track Selector series. The TS and NTS have a limited angle acceptance, and then search a specific track in a view. The UTS began to search all of recorded tracks with the angle of $\tan \theta < 0.6$.

The stage driving method has also been improved. Until the UTS, after the step movement of the XY -axis stage with motors to an aimed position, tomographic images were taken by changing the focal plane along the optical axis, i.e. Z axis. There is a dead time to wait for a

settlement of a vibration of the XY -axis stage. The vibration is caused by the acceleration and de-acceleration of XY -axis stage, so continuous stage movement has been adapted to S-UTS. A dual piezo driven objective lens has been installed; Z axis is to change the focal plane, and X axis is to cancel the X -axis stage movement. As a result, the step and go movement of X -axis stage has been removed. The continuous stage movement overcame a bottle neck for the speed up. In addition, a high frame rate camera of 3000 frame/s increased the readout frequency to 50 view/s, which is more than 10 times faster than the previous system. FPGA-based processors for high-speed image processing have also been developed to handle this high data rate.

However, further speed up along this direction; continuous stage movement with high frequency movement of the objective lens, seems unrealistic, because the acceleration becomes $\sim 100 \text{ m/s}^2$ if we intend to achieve the readout frequency of 500 view/s. Therefore, we changed the strategy from increasing the readout frequency to widening the field of view (FOV) for a new Track Selector, HTS. To serve this purpose, we have developed a dedicated objective lens with the FOV of 5.1 mm square, which is about 500 times wider than the previous system. In order to cover this wide FOV with the resolution of sub-micron, a mosaic camera system composed of 72 two-megapixel sensors have been developed. The wide FOV is read by 72 sensors in parallel and each taken images have to be processed within the time comparable to that for stage movement. Because the step motion was adapted again, the vibration bottleneck relapsed described above. Hence, a counter stage was introduced to cancel the movement and then to hold the center of gravity of the stage, which seems to be the origin of the stage vibration. A linear motor has been adapted to move the stage at a high acceleration and deceleration. We also adapted consumer GPUs for the image processing and track recognition. The GPUs are readily available, widely used and have design flexibility.

Fig. 3 shows a picture of HTS system, dedicated lens, camera, XYZ -axis stage mounted on a base, and computer cluster for image processing. The details of each part will be described in the next section.

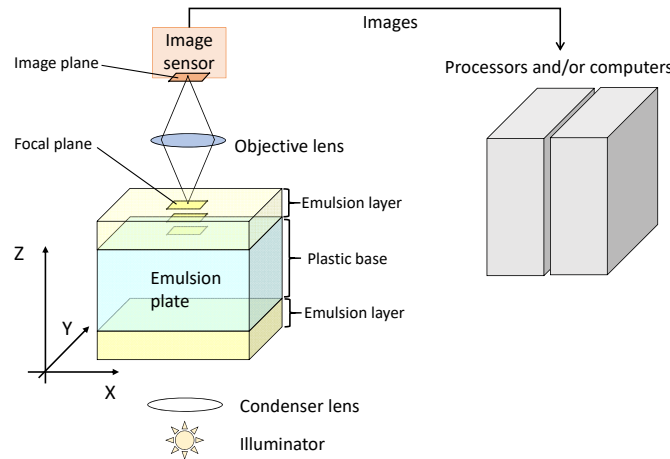


Fig. 1: Outline of a nuclear emulsion automatic readout system

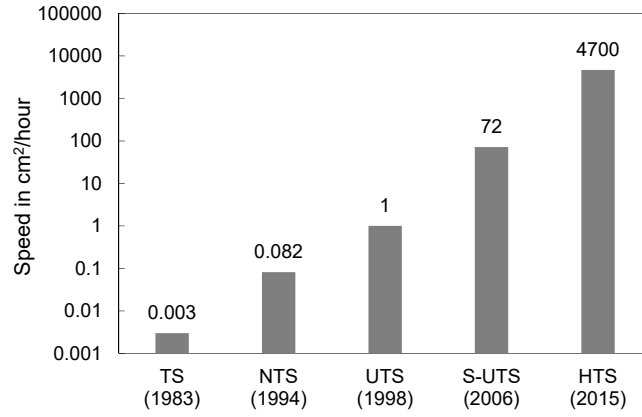


Fig. 2: Development of the scanning speed of the Track Selector series. The values of TS and NTS are the speed at the same angular acceptance as UTS.

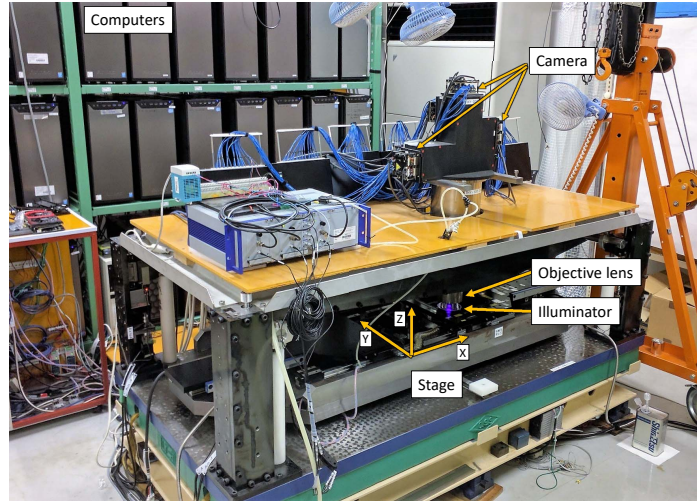


Fig. 3: Picture of HTS.

3. The HTS system

3.1. Optics: Objective lens and illuminator

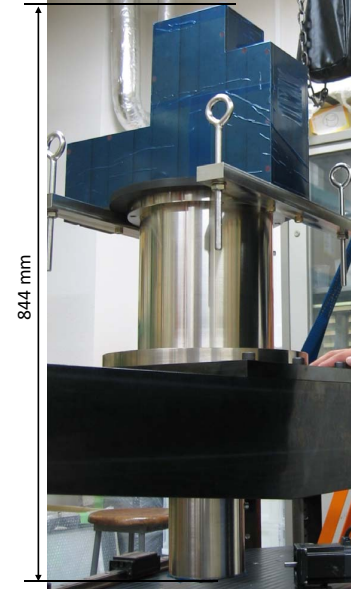
The optics, i.e. objective lens, illuminator and beam splitter was designed and produced by KONICA MINOLTA Inc. The specifications are shown in Table 1 and the outlook is shown in Fig. 4. The FOV is 5.1 mm square, the magnification is $12.1\times$ and the working distance is 1.5 mm. Optical immersion oil with a refractive index of 1.505 must be inserted between the objective lens and the emulsion plate for optical matching.

In order to produce the wide view objective lens with a reasonable cost, the numerical aperture (NA) is limited to 0.65. The NA is lower than 0.85 of the previous objective lens with the FOV of 0.2 mm square. In order to recover the degraded optical resolution by the smaller NA, light with wavelength λ of 436 nm is utilized, which is shorter than 550 nm of the previous. The wavelength shorter than 400 nm can not be adapted due to the smaller transmittance of the material used for nuclear emulsion. The lateral resolution defined by

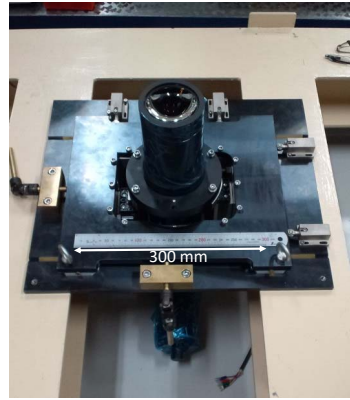
Rayleigh criterion ($\delta x = 0.61 \frac{\lambda}{NA}$) became 410 nm. The resolution is almost same as that of the previous lens of 390 nm. As a light source, a mercury xenon lamp are used to obtain enough brightness on the whole FOV and band-pass optical filters centered at 436 nm with FWHM of 10 nm are used to ignore chromatic aberration. Also because of the smaller NA, the depth of field (DOF) ($\delta z = 2 \frac{\lambda}{NA^2}$), i.e. the resolution along the optical axis, became $2.1 \mu\text{m}$ which is about 1.5 times wider than that of the previous lens.

	S-UTS	HTS
Objective lens		
Manufacture	TIYODA	KONICA MINOLTA
Magnification	$35 \times$	$12.1 \times$
Numerical aperture	0.85	0.65
Optimum wave length	Green (550 nm)	Blue (436 nm)
Working distance	1.1mm	1.5 mm
Depth of field	$1.5 \mu\text{m}$	$2.1 \mu\text{m}$
Field of view	$0.230 \times 0.228 \text{ mm}^2$	$5.1 \times 5.1 \text{ mm}^2$
Illuminator		
Condenser NA	0.85	0.66
Light source	Hg-Xe lamp	Hg-Xe lamp
Filter	Green filter	$436 \pm 10 \text{ nm}$

Table 1: Specifications comparison of the objective lens and illuminator between S-UTS [11] and HTS. The depth of field is defined as $\delta z = 2 \frac{\lambda}{NA^2}$.



(a) Objective lens and beam splitter



(b) Condenser lens for the illuminator

Fig. 4: Photos of the optics.

3.2. Camera

HTS uses 72 image sensors. As shown in Table 2, one sensor has 2.2 megapixel (2048×1088 pixels). The physical pixel pitch of $5.5 \mu\text{m}$ is corresponding to $0.45 \mu\text{m}$ on the object. This value of $0.45 \mu\text{m}$ is almost equal to the diffraction limit of $0.41 \mu\text{m}$ as described in section 3.1.

Six mosaic camera modules, in which 12 image sensors are arranged respectively as shown in Fig. 5, are installed on the six image planes divided by the beam splitter. Each camera covers different part of the view of 5.1 mm square as shown in Fig. 6 and has overlap of more than $50 \mu\text{m}$ (at object) with the adjacent sensor in order to have a tolerance for an alignment error and not to miss the trajectory at the sensor edge.

The frame rate of the sensor is 300 frame/s which is ten times slower than that of S-UTS. The total image transfer rate is 48 GB/s, which is 60 times larger than that of S-UTS.

Image sensor	S-UTS	HTS
Product name	MEMCAMfx RX-6 custom	CMV2000
Image sensor	CMOS	CMOS
Resolution	512×508 pixels	2048×1088 pixels
Frame rate	3000 fps	300 fps
Pixel pitch	$16 \mu\text{m} \times 16 \mu\text{m}$	$5.5 \mu\text{m} \times 5.5 \mu\text{m}$
Electronic shutter	Available	Available

Table 2: Specifications comparison of the image sensor between S-UTS [11] and HTS.

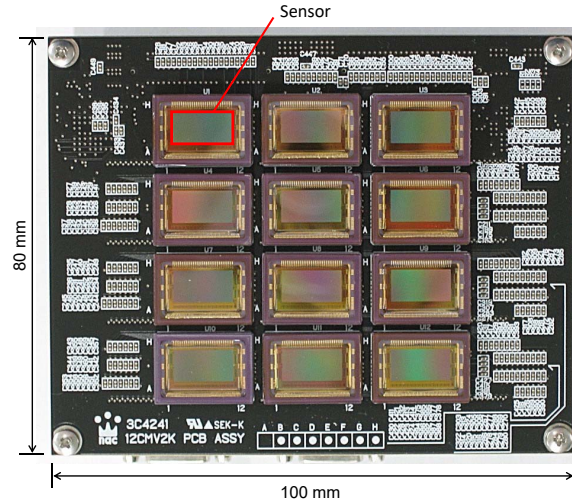


Fig. 5: Photo of mosaic camera unit. Twelve image sensors are mounted on one unit. The red bold frame shows the sensitive part of a sensor.

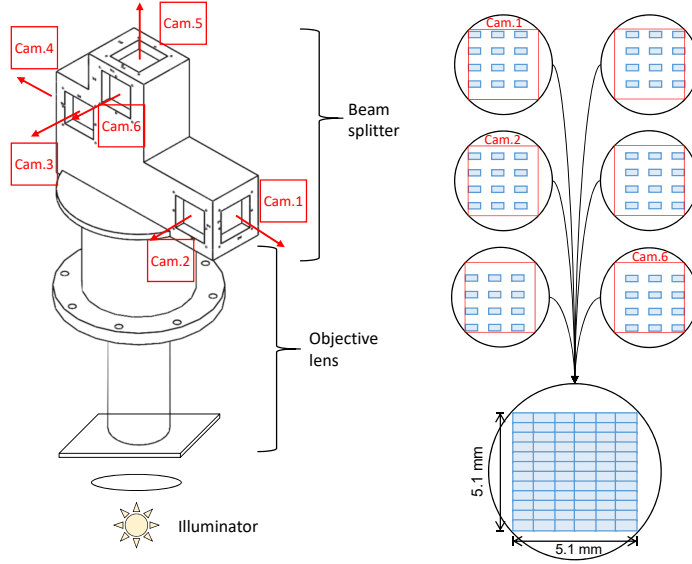


Fig. 6: Schematic view of the beam splitter unit with six windows (left) and the configuration of field of view constructed with six mosaic camera units (right).

3.3. *XYZ-axis stage*

3.3.1. *XY-axis stages.* The *XY* stage is set on a metal surface table of which size is $2 \times 1 \text{ m}^2$ and weight is about 700 kg. The stage stroke is matched up to the OPERA film of which size is $125 \times 100 \text{ mm}^2$ [20]. *X* direction is designed to be the main scanning direction and the stroke is set to be 130 mm. The *X* stage is driven by a linear motor, which has a capability to drive 5 mm step movement of the 35 kg *X* stage in 20 msec. As shown in Fig. 7, a counter stage is installed and then the counter stage is driven to suppress the vibration caused by the movement of the center of gravity of the system. The stroke of *Y* stage is set to be 100 mm. The *Y* stage is driven by a rotary motor and a ball screw. Three linear encoders are installed on each stage (two on *X* and one on *Y*), and the encoders are used to monitor the stage position and to feedback to each actuator.

3.3.2. *Z-axis stage.* *Z* stage has two driving mechanics, i.e. coarse lens movement and fine film movement. The coarse lens movement drives the lens and its support weighting 200 kg to change the emulsion layers and to exchange the scanning films. The coarse movement consists of four rotary motors equipped with rotary encoders and ball screws and the stroke is set to be 20 mm. The fine film movement drives the film to acquire tomographic images of an emulsion layer. The fine movement consists of piezo actuators which have linear encoders for the feedback of the *Z* position.

3.4. *Computer clusters*

3.4.1. *Computer configuration.* The HTS system configuration is shown in Fig. 8. The system is controlled by 38 computers, i.e. one main computer, one data storage computer and 36 tracking computers.

The main computer controls stage movement through motion controller and piezo controller. There are 72 image sensors in 6 camera units covering $5.1 \times 5.1 \text{ mm}^2$ FOV. Each

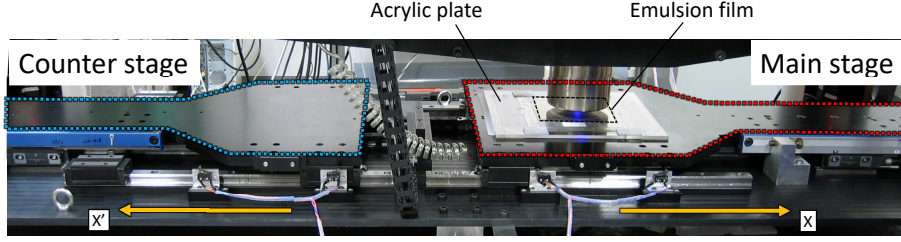


Fig. 7: Configuration of X -axis stage. The main stage and the counter stage are installed in line and are driven to the opposite direction to keep the center of gravity at rest.

sensor is connected to a sensor controller, and one GPU board (NVIDIA GeForce GTX680 or higher) is used for image processing and track recognition per one sensor. Two sensor controllers and two GPU boards are mounted on one tracking computer. Then, 36 tracking computers cover all the 72 sensors.

Network configuration of those computers is shown in Fig. 9. Main computer, tracking computers and data storage computer are connected through Ethernet. The main computer and the tracking computers are connected through 1 Gigabit Ethernet (GbE). The main computer triggers data taking sequence of the tracking computers and receives feedback information like the number of recognized grains from the tracking computers in order to monitor the status of data taking. Recognized track data is transferred from tracking computers to a storage computer. The storage computer are connected through 10 GbE in order to deal with the data simultaneously transferred from 36 tracking computers. After storing the data on the storage computer, analysis computers reconstruct tracks from the output data as offline analysis. The analysis computer also connects with 10 GbE to copy the data from the data storage computer.

3.4.2. Software configuration. The software configuration is shown in Fig. 10. Scan manager, stage manager, piezo manager, shutter manager are in operation on the main computer. Track recognition program and sensor manager are in operation on the tracking computers. The images used in the tracking recognition program are transferred from the sensor manager via the shared memory.

3.5. Track recognition procedure

Twenty two tomographic images are taken by changing the focal plane through the emulsion layer, and sixteen successive images in emulsion layer are used for the track recognition. A typical thickness of an emulsion layer is $60\text{ }\mu\text{m}$.

3.5.1. Image processing. Image processing applied to the original images has two steps. The two steps are performed on the GPUs and are using OpenCV library (version 2.4).

The first step is an extraction of focused grains on the images. A low-pass filter is applied to the original image to make blurred background image. A grain has a typical size of $0.5\text{ }\mu\text{m}$ which corresponds to about one pixel on the image. So the cutoff frequency of the low-pass filter should be approximately $1/(10\text{ pixels})$. The background brightness $B_{BG}(x, y)$ for a pixel (x, y) is calculated by averaging the weighted brightness of $N \times N$ pixels surrounding

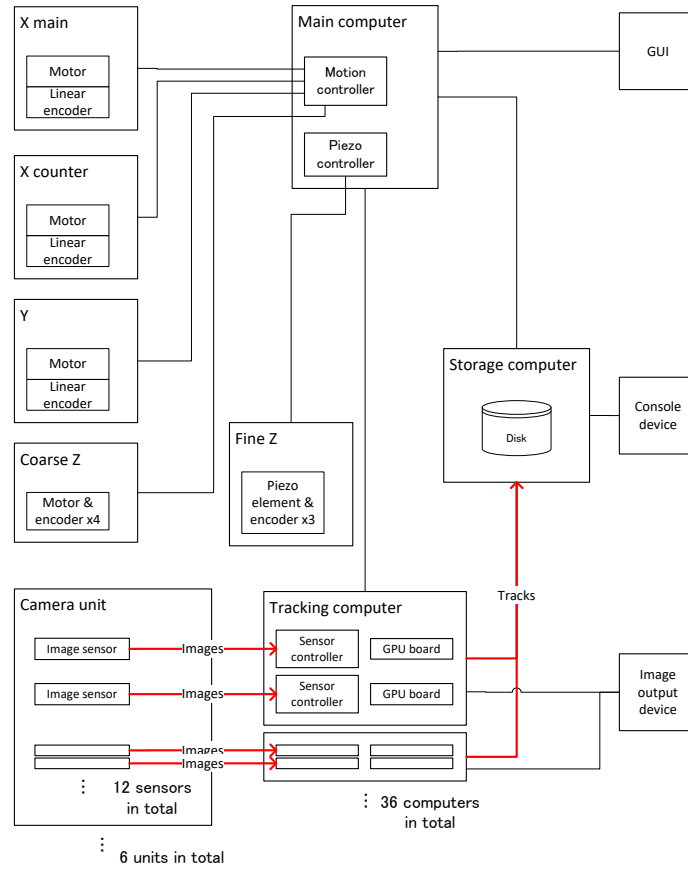


Fig. 8: Schematic view of the HTS system configuration.

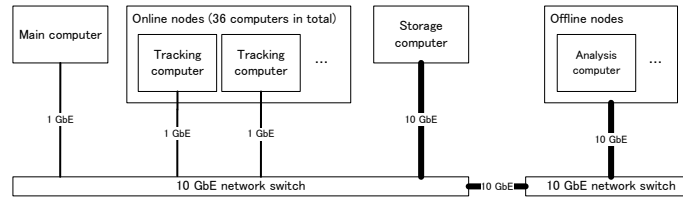


Fig. 9: Network configuration of the HTS system.

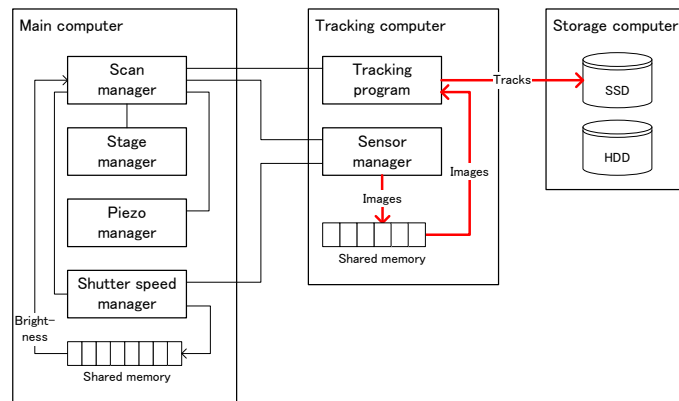


Fig. 10: Software configuration of the HTS system.

a specified pixel of original brightness $B_{Original}$ with a matrix, i.e. a kernel K .

$$B_{BG} = \sum_{i=1}^N \sum_{j=1}^N B_{Original}(x+i, y+j) \cdot K(i, j).$$

We used the cutoff frequency of $1/(12.5 \text{ pixels})$ and the kernel with 15×15 matrices. By subtracting this averaged image from the original image, the image with high frequency component is obtained as shown in Fig. 11. Finally, by applying threshold cut, we obtained the grains on the images.

At the second step, elimination of off focus grains spread over the images with different focal depth is applied. This process was performed to a certain image of a layer k with the images before and after layers $k \pm 1$.

$$B'_k = B_k - \frac{a}{2} (B_{k-1} + B_{k+1}).$$

The factor a was adjusted so that the spread of focused grains was less than the interval of the images. After those processes, a threshold cut is applied to get binary images. And then, hit expansion of 2×2 (Fig. 12 (b)) or 3×3 (Fig. 12 (c)) is carried out, because the size of the grain hit is normally smaller than the allowance of the trajectory recognition algorithm. We usually utilized 2×2 expansion.

3.5.2. Judgement of the success of the image acquiring. The judgement, whether the acquired tomographic images cover an emulsion layer adequately or not, should be done before the movement to the next field of view. In the standard setting, 22 images are captured and sixteen successive images are used for track recognition and then six images for margin layers.

The number of grains (NOG) recognized in each layer is calculated by the image processing step 1. The existence of the emulsion layer in the image layers is judged when the NOG is larger than a defined threshold.

Because of the wide FOV and multiple sensors, the emulsion layer locations of each sensor are spreading in about two layers among 22 image layers. As shown in Fig. 13, using NOG information, the end layer is calculated for each sensor. An average value of the margin layers over all sensors is calculated using the obtained all the end layers. If the average value of the margin layers is less than 1, the image data taking is re-tried. And if the average value is greater than 1 and less equal to 1.5, the Z position to start image taking is corrected in the next field of view. By those treatments, minimization of the time loss due to the re-data taking is achieved.

3.5.3. Track recognition. Straightly aligned grains through the sixteen binarized tomographic images are searched with the method described in the previous paper [11]. The method, so-called Track Selector algorithm, uses simple shift and sum functions. The binary images are shifted to X and Y as the specified angle tracks become perpendicular to the focal plane and summed perpendicularly. The sum up value called Pulse Height (PH) is an indicator of the track-likelihood. Then by setting the threshold, tracks which have the specified angle are recognized. The process is repeated by changing the angle specification, i.e. scanning the required angular range. The relative shift value from first layer to sixteenth layer is given to be every three pixels ranging of ± 180 pixels for X and Y individually in

the case of standard condition. The corresponding angle range is ± 53 degree in the case of $60\text{ }\mu\text{m}$ thick emulsion layer. Although the readout speed becomes slower, we can choose the relative shift pixel ranging of ± 360 pixels, i.e. the corresponding angle range of ± 70 degree. This tracking program can handle up to $\sim 10^6$ tracks/cm² without extra processing time. The speed-up of this tracking programs installed in the GPU is one of the key to realize HTS. The details will be described in future paper.

After applying threshold cut, clustering of the recognized tracks in angle and position space is applied because one track has multiple hits spreading over the angle and position space. The clustering process is performed by the CPU of the tracking computer. At this clustering process, volume of the hits over the position space ($PHvol$) is also calculated, which is representing the darkness of the track, i.e. the size of ionization energy loss per unit length (dE/dx). The finally identified track is called a micro track and is the base for further track reconstruction.

3.5.4. Diagram of the procedure. The time chart for scanning is shown in the Fig. 14. Except at the time of judgment, the stage, the camera, and the tracking computers work in parallel. In the standard setting of track recognition, the time of moving to the next view is longer than the total of image processing step 2 and track recognition.

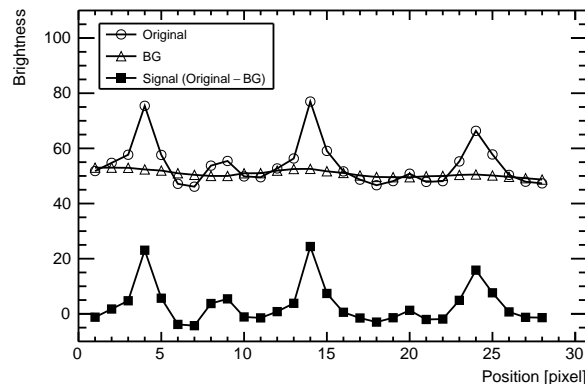


Fig. 11: Schematic view of the image processing to extract grains. The low frequency background BG is extracted from the original image. Grains are appeared as the peaks in the signal which is the BG subtracted from the original.

4. Sensor to sensor alignments

Unification of the 72 independent image sensors into one coordinate is the first attempt in the history of nuclear emulsion readout system.

The objective lens has a distortion like “Radial distortion” in its wide view of $5.1 \times 5.1\text{ mm}^2$. Although this distortion thought to affect the position and angle of the recognized tracks, the effects can be ignored because of the fine segmentations of the FOV into 72 sensors; an affine transformation parameter of each sensor can correct the magnification difference and position offset for each sensor.

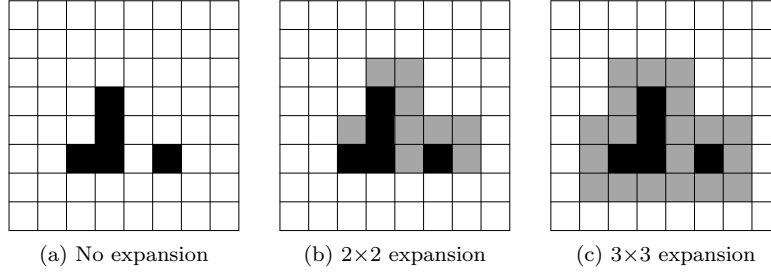


Fig. 12: Schematic view of the image expansion. The original pixels and the expanded pixels are the black pixels and the gray pixels, respectively.

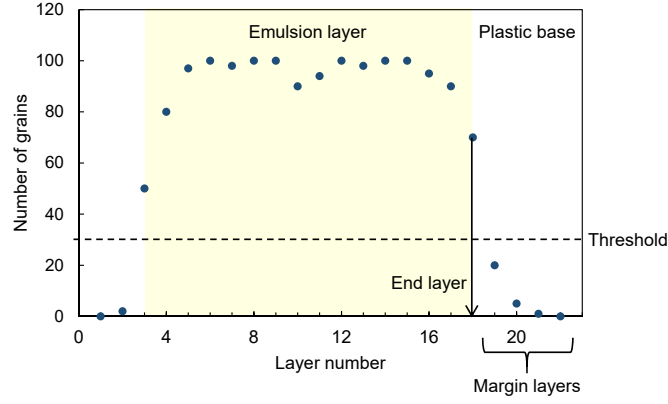


Fig. 13: Method to locate emulsion layer position among tomographic images.

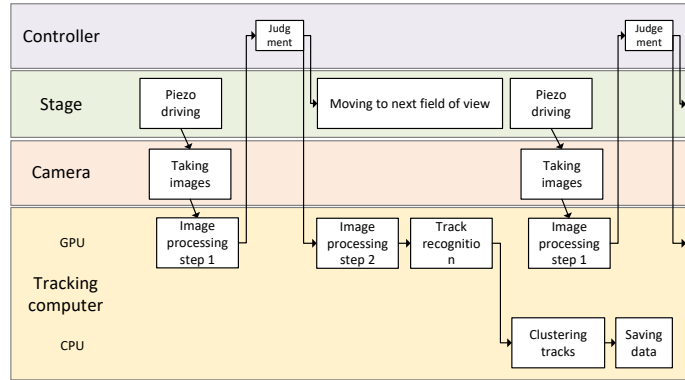


Fig. 14: Time sequence of each device activity. The length of the squares is not proportional to the actual time.

The coordinate system of each sensor should be unified into the stage coordinate based on the encoders of the XYZ -axis stage. For the coordinate transformation from each sensor coordinate to the stage coordinate, affine parameter (a_i, b_i, c_i, d_i for rotation and deformation correction, and p_i, q_i for displacement correction) should be defined. Here p_i and q_i are defined relative to one reference sensor.

$$\begin{pmatrix} x \\ y \end{pmatrix} = \begin{pmatrix} a_i & b_i \\ c_i & d_i \end{pmatrix} \begin{pmatrix} px_i \\ py_i \end{pmatrix} + \begin{pmatrix} p_i \\ q_i \end{pmatrix}.$$

4.1. Sensor alignment using grains recorded in a real emulsion

In order to determine the affine parameters of each sensor, real grains contained in a nuclear emulsion are used like the calibration of segmented sensors of a telescope using a star catalog. Calculation of affine parameters is performed as follows. At first, a_i – d_i are obtained by comparing the amount of movement in a sensor coordinate and stage coordinate by moving the stage to the X and Y direction. Secondary, a main grain catalog of $5 \times 5 \text{ mm}^2$ is created by using a reference sensor, and sub grain catalogs of $1 \times 0.5 \text{ mm}^2$ are created by using the other sensors. These catalogs are corrected by using a_i – d_i obtained in the above procedure. Finally, the displacement parameter of p_i and q_i can be obtained by comparing each sub catalog to the main catalog. These catalogs are revised when the parameters are re-measured.

The magnification ($mag = \frac{1}{2} (\sqrt{a^2 + b^2} + \sqrt{c^2 + d^2})$) is $0.4545 \text{ } \mu\text{m}/\text{pixel}$ on average of all the sensors. The ratio of mag to the minimum one is shown in Fig. 15. The maximum mag is 0.39% larger than the minimum mag by the radial distortion and these two sensors are 3.0 mm apart. This corresponds to radial distortion of 0.234% from the center to the corner of the FOV. By this value, the distortion of a $80 \text{ } \mu\text{m}$ long track which is the longest track in the standard setting is calculated to be 0.1 pixels, which is found to be sufficiently smaller than the required value of one pixels.

4.2. Calibration method by using real scanning data

Those affine parameters are sometimes shifted by aging and/or thermal expansion of the camera support and so on. As there are overlap areas (27% in area) between sensors, a trajectory in the overlap area is detected at a couple of positions when the sensor position changes.

As the method described in section 4.1 is quite time consuming, a method using real track data was devised. In order to determine the relative displacement of each sensor, the position displacement vector (D_1, D_2, D_3, D_4) relative to the four adjacent sensors are calculated respectively for each sensor by comparing the position difference of those simultaneously recognized tracks. Then the most probable relative displacement vector $P_i(x, y)$ are calculated by minimizing the residuals σ defined as:

$$\sigma^2 = \sum_{i=1}^{72} \sum_{j=1}^4 (D_{ij} - P_i)^2,$$

by analytical calculations assuming P_1 to be $(0, 0)$, where i is the sensor number. The residuals are calculated in the X and Y directions independently. After this process, the track positions are converted again with the new affine parameters. And then the distribution of the position difference of the tracks in all of the adjacent sensors was obtained as shown in Fig. 16. The sigma of dx and dy are obtained to be 0.23 and 0.26 μm for X and Y axis respectively. This accuracy is precise enough to the pixel size of 0.45 μm .

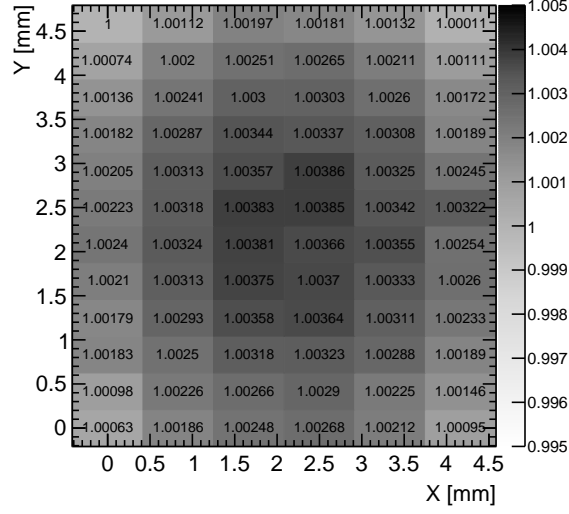


Fig. 15: Magnification ratio of each sensor. The minimum value is appeared at the most upper left sensor and is set to one.

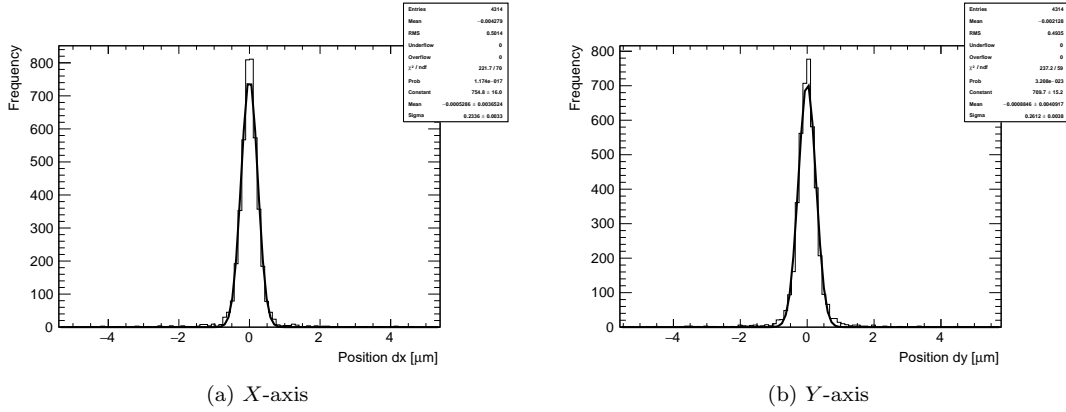


Fig. 16: Distribution of position difference of the tracks recognized in overlap area of the two adjacent sensor.

5. Stage tuning

Since HTS has utilized step movement (go and stop) to scan films and the distance of the step has been order of magnitude longer, the vibration effect caused by the stop movement should be well understood. The residual vibrations after stop may cause blurred grain images or curved tracks, and then the pulse height may be decreased and the recognized position and angle may be shifted.

5.1. Evaluation of the vibration effect

In order to evaluate the vibration, 30 images (=0.1 seconds) were taken with fixing the Z position from the moment when the encoder of the X -axis stage reaches the target position. Using grains recognized in the captured images, positional deviations between sequential frames were measured.

5.2. Result

At first, the maximum velocity was fixed to be 100 mm/s and the acceleration was varied from 1.0–10 m/s². The counter stage was driven to be synchronized to the main stage. When the acceleration was greater than 5 m/s², the vibration was not settled within 0.12 seconds. Therefore we set the acceleration as 5 m/s². Next, we evaluated the difference between with and without the counter stage movement. The result is shown in Fig. 17. The amount of vibration is significantly reduced with the counter stage movement.

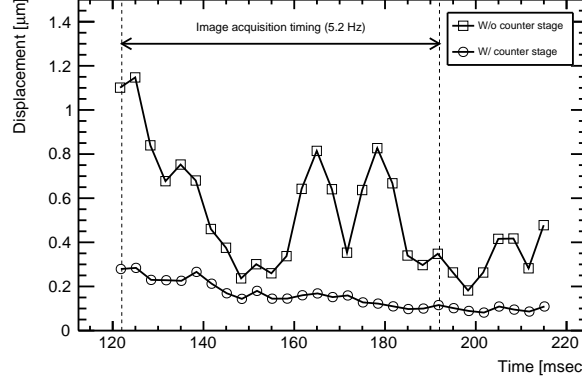


Fig. 17: Effect of the counter stage. Circle and square shows the vibration in the case of with and without the counter stage movement respectively.

6. Evaluation

6.1. Overview of the performance evaluation

The performance of an automatic readout machine is evaluated mainly by track finding efficiency and angular accuracy. In this time, we evaluated the HTS performance by using real data of the nuclear emulsion films exposed in GRAINE 2015 flight [21]. The films have a size of 25×38 cm². About 60 μm thick emulsion layers were coated on both sides of a 180 μm thick polystyrene plastic base. The density of silver bromide crystals in the emulsion is higher than that of OPERA film [20] which was used in S-UTS evaluation. All of the films contained in the converter section and the shifter section were readout by the HTS. For this evaluation, only the bottom three films of the convert section of the area of 117 cm² were used. The quality of converter and shifter section will be discussed in another paper.

In GRAINE 2015 flight, the nuclear emulsion has a history of 8.5 days on the ground and 14.4 hours on the flight. Among the flight, the level flight at the altitude of 37.2 km was continued for 11.5 hours.

6.1.1. Track reconstruction. Micro tracks of two emulsion layers on both side of a plastic base are connected, and then a base track candidate is made. As shown in 18 (a), we have connected the edges of two micro tracks on base side to make the angle and position of the base track. The PH of base track is summed PH of two micro tracks. We have defined that more likely base track has smaller angular difference between each micro track and the base track.

Because the angle of a micro tracks \vec{ma} is affected by the shrinkage and the distortion of the emulsion layer caused by the development, those effect should be corrected by using so-called shrinkage factor shr and distortion vector \vec{dist} as:

$$\vec{ma}' = shr \cdot \vec{ma} + \vec{dist}.$$

Here, \vec{ma} is the original angle and \vec{ma}' is the corrected angle. The shrinkage factor and distortion vector are calculated to maximize the number of connected base tracks. The base tracks crossing multiple films are reconstructed with the angle and position consistency as shown in Fig. 18 (b).

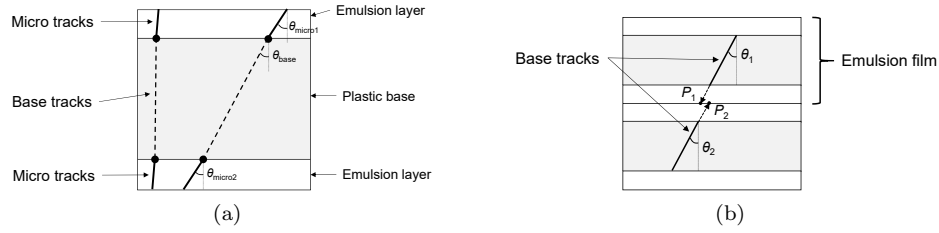


Fig. 18: (a) The definition of micro track and base track. (b) The definition of the angle and position difference between two base tracks. The angle difference is $|\theta_1 - \theta_2|$ and the position difference is $|P_1 - P_2|$.

6.2. Results

6.2.1. Base track finding efficiency. In order to evaluate the track finding efficiency at a film, tracks were reconstructed by using the films sandwiching the target film, and the existence of the reconstructed tracks was checked at the target film. Base track finding efficiency of a film is defined as a ratio of the number of found predicted tracks to the number of all predicted tracks.

The measured angular dependence of the track finding efficiency is shown in Fig. 19. The efficiency was greater than 97% in the angular range of $\tan \theta < 1.6$. The efficiency for $\tan \theta$ less than 0.2 is slightly higher than other regions. The angle dependence of pulse height is shown in Fig. 20 (a). The efficiency seems to correlate to the average PH. The PH distribution of the found tracks for $0.0 < \tan \theta < 0.1$, $0.2 < \tan \theta < 0.3$ and $0.9 < \tan \theta < 1.0$ are shown in Fig. 20 (b). The PH average for $0.0 < \tan \theta < 0.1$, $0.2 < \tan \theta < 0.3$ and $0.9 < \tan \theta < 1.0$ was measured to be 31.2, 28.5 and 25.4 respectively.

6.2.2. The angular accuracy. The angular accuracy of the micro tracks is defined as the angular difference between the micro tracks and the base tracks. And that of base tracks is defined as the angular difference between the base track in the evaluating film and that in the next film. As shown in Fig. 21, the angular accuracy was resolved for “radial and lateral” components; the radial axis is the horizontal direction of the track, and the lateral axis is the perpendicular direction. Because the depth of field is larger than the lateral resolution, the two components are very different in the large angle tracks. The angle dependence of angular accuracy of micro tracks is shown in Fig. 22 and that of base tracks is shown in Fig. 23.

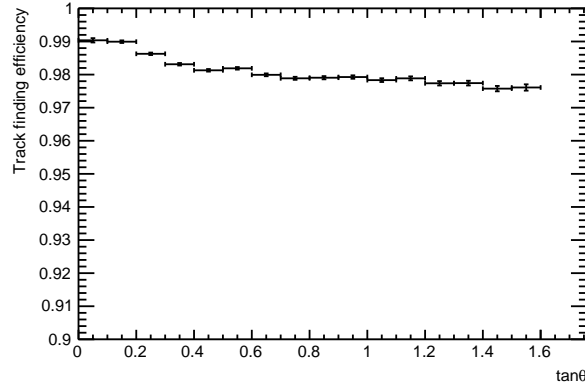


Fig. 19: Angle dependence of the track finding efficiency of base tracks.

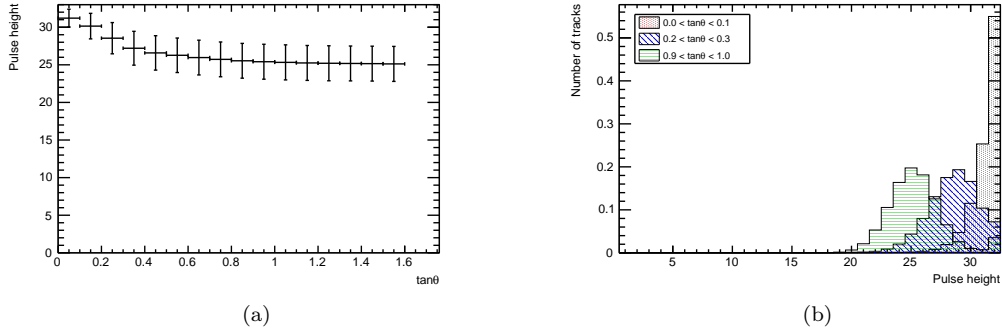


Fig. 20: (a) Angle dependence of average pulse height of the base tracks. The error of the average is a standard deviation. (b) Pulse height distributions of the base tracks of $0.0 < \tan \theta < 0.1$, $0.2 < \tan \theta < 0.3$ and $0.9 < \tan \theta < 1.0$.

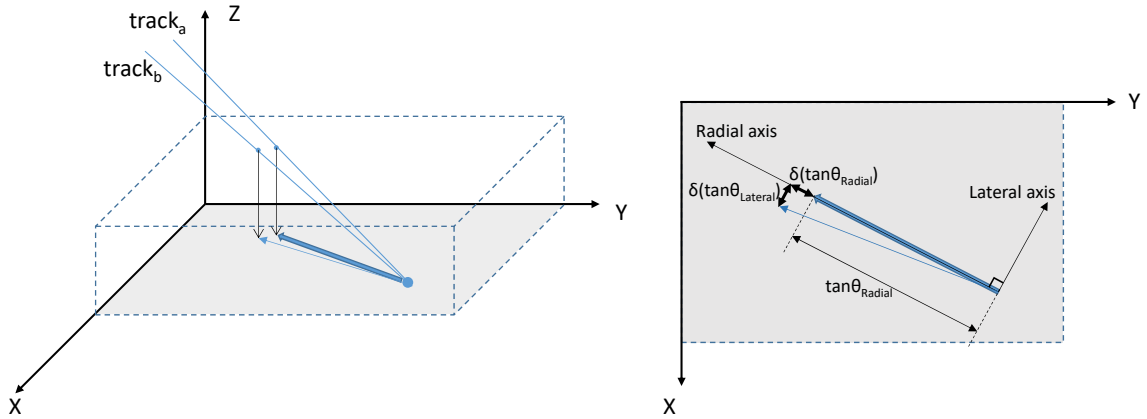


Fig. 21: Schematic view of the definition of “Radial-Lateral” components of angular difference between two tracks.

6.2.3. *The track finding efficiency dependence of readout repetition frequency.* The repetition frequency in the above evaluation was 4.2 view/s, which corresponds to a readout speed of 3800 cm²/h.

We investigated the track finding efficiency as a function of the repetition frequency from 4 view/s to 5.5 view/s. The frequency was changed by changing the timing to the start image data taking, while the peak speed and the acceleration of X -axis stage were not changed. The result is shown in Fig. 24. The efficiency becomes lower when the frequency becomes higher. For example, the efficiency was deteriorated by 1% in the case of the track with angle of $0.9 < \tan \theta < 1.0$ when the frequency was changed from 4.0 view/s to 5.2 view/s. If you can accept 1% decrease, the readout speed of 4700 cm²/h at the 5.2 view/s can be executed.

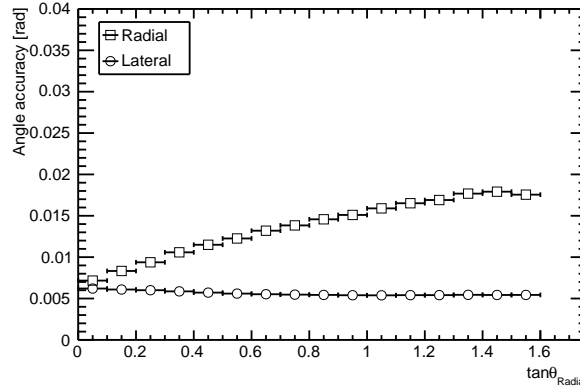


Fig. 22: Angle dependence of angle accuracy for micro tracks.

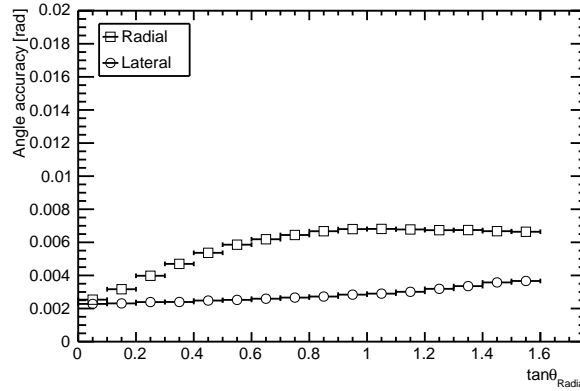


Fig. 23: Angle dependence of angle accuracy for base tracks.

6.3. Discussion

The reason, why the pulse height of smaller angle track is higher, is in the focal depth. The distance of image data taking in Z direction is determined to be almost same value as the

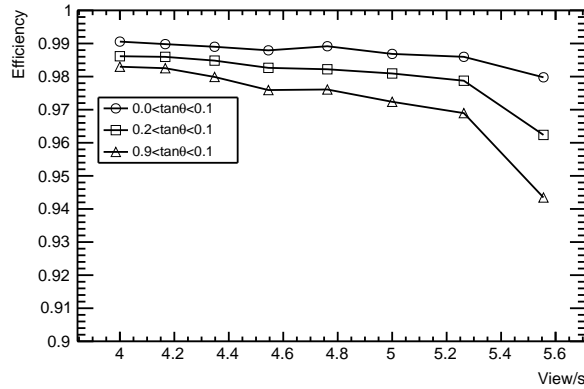


Fig. 24: Dependence of the track finding efficiency for the readout speed. Here, 5.2 view/s corresponds to 4700 cm²/h.

focal depth of the HTS about 4 μ m. When two grains are lined up in the direction of the optical axis, the grain image spreads over images of the different depths. As a result, it is considered that PH is amplified at a smaller angle.

The angular accuracy of micro tracks of HTS seems better than that of S-UTS [11]. This improvement is probably caused by the better sensitivity of the GRAINE emulsion. The angular accuracy of the base tracks in small angle is almost same as that of S-UTS. On the other hand, the angular accuracy in larger angle seems a little bit worse. The reason is that the GRAINE film is incident with cosmic rays in various energies, but the films for S-UTS evaluation are irradiated with 150 GeV/c muon beam.

In order to improve the angular accuracy of the base track even at a large angle, it is necessary to improve the position accuracy of the Z direction. When acquiring images, since the clocks of 72 sensors are not synchronized, the focal plane has an error about the distance 4 μ m of taking images. Furthermore, the image of one grain has an error of 4 μ m in the depth direction because of the focal depth. Implementation of synchronous signals and advance of image processing will solve the angular accuracy problem.

At the HTS, we have improved the readout speed by widening the field of view. As described in section 2, in order to increase the readout speed, there are two direction; one is to increase the frequency of readout repetition and the other is to widen the FOV. HTS took the second way. For further speed-up, we are designing a new readout system HTS-2 along the both directions. An objective lens with twice wider FOV and a contentious movement with a diagonal focal plane will be adapted. HTS-2 is aiming at the scanning speed of 25000 cm²/h, which is about 5 times faster than the HTS (HTS-1).

7. Conclusion

Nuclear emulsion is a three dimensional particle tracking detector with more than 100 years history, still it has extensive application field developed by the invention of automatic nuclear emulsion readout system. The newest machine HTS, described in this paper intends to deal with those modern applications. HTS have been developed with a wide field lens of 5.1×5.1 mm² field of view and 72 two-megapixel sensors to cover this field of view. We also

applied 72 GPUs and 36 CPUs for image processing. 5.2 view/s scanning with 5 mm step movement has been achieved by utilizing the counter stage. Finally HTS achieved readout speed of about 0.5 m²/h, which is almost two order faster than the previous system used in OPERA experiment. This speed is corresponding to the scanning area of ~ 1000 m²/year.

There are two main subjects for HTS. One is a wide field parallel readout by multi sensors keeping sub-micron accuracy. The other is a vibration suppression after the step movement. As described above, the new method for multi-sensor position alignment has been accomplished by using real grain and track data. For the vibration suppression, the realistic acceleration value was tuned by using counter stage.

Until today, HTS has readout an area of about 50 m² of GRAINE 2015 flight, shows that the tracking efficiency is greater than 97% for the tracks with the angle of $\tan \theta < 1.0$ and is contributing to the observation of cosmic gamma-rays. Relating to muon radiography, an area of about 80 m² has been readout and new inner structures are identified in Pyramids. In NINJA project, HTS has readout an area of about 20 m² and is contributing the study of low energy neutrino interactions. Also the availability of HTS stimulates new projects, triggers a new collaborative work and HTS is becoming an indispensable tool in future radiation measurements.

Acknowledgment

We would like to thank T. Kawai for constructing HTS. We wish to acknowledge valuable discussion on calibration method with S. Kukita. This work was supported by JSPS KAKENHI Grant Numbers JP22340057, and the JST-SENTAN Program from Japan Science and Technology Agency, JST. A part of instruments was supported by Kobayashi-Maskawa Institute for the Origin of Particles and the Universe (KMI). M. Yoshimoto and H. Kawahara were supported by Grant-in-Aid for JSPS Research Fellow. I thank all the collaborators who have utilized the HTS for their experiments.

References

- [1] R. Brown et al., *Nature*, **163**, 82 (1949).
- [2] K. Niu et al., *Progress of Theoretical Physics*, **46**(5), 1644–1646 (1971).
- [3] K. Niwa et al., the proceedings of the International Cosmic ray Symposium of High Energy Phenomena, Tokyo, p. 149 (1974).
- [4] S. Aoki et al., *Nucl. Instrum. Meth.*, **B51**, 466–472 (1990).
- [5] T. Nakano, Ph.D. Thesis, Nagoya University, Japan (1997) (in Japanese).
- [6] J. P. Albanese et al., *Phys. Lett.*, **B158**, 186–192 (1985).
- [7] K. Kodama et al., *Nucl. Instrum. Meth.*, **A289**, 146–167 (1990).
- [8] S. Aoki et al., *Prog. Theor. Phys.*, **85**, 1287–1298 (1991).
- [9] E. Eskut et al., *Nucl. Instrum. Meth.*, **A401**, 7–44 (1997).
- [10] K. Kodama et al., *Phys. Lett.*, **B504**, 218–224 (2001), arXiv:hep-ex/0012035.
- [11] K. Morishima and T. Nakano, *JINST*, **5**, P04011 (2010).
- [12] R. Acquafredda et al., *New J. Phys.*, **8**, 303 (2006), arXiv:hep-ex/0611023.
- [13] N. Armenise et al., *Nucl. Instrum. Meth.*, **A551**, 261–270 (2005).
- [14] N. Agafonova et al., *PTEP*, **2014**(10), 101C01 (2014), arXiv:1407.3513.
- [15] N. Agafonova et al., *Phys. Rev. Lett.*, **115**(12), 121802 (2015), arXiv:1507.01417.
- [16] S. Aoki et al. (2012), arXiv:1202.2529.
- [17] S. Takahashi et al., *PTEP*, **2016**(7), 073F01 (2016).
- [18] WB Atwood et al., *The Astrophysical Journal*, **697**(2), 1071 (2009).
- [19] T. Fukuda et al. (2017), arXiv:1703.03659.
- [20] T. Nakamura et al., *Nucl. Instrum. Meth.*, **A556**, 80–86 (2006).
- [21] K. Ozaki et al., *JINST*, **10**(12), P12018 (2015).